Nanostructured magnetoceramics from hyperbranched polymer precursors

Qunhui Sun [a], Kaitian Xu [a], Jacky W.Y. Lam [a], John A.K. Cha [a], Xixiang Zhang [b],
Ben Zhong Tang [a, *]

[a] *Department of Chemistry, Hong Kong University of Science and Technology, Clear Water Bay, Kowloon, Hong Kong, China*
[b] *Department of Physics, Hong Kong University of Science and Technology, Clear Water Bay, Kowloon, Hong Kong, China*

Abstract

Controlled pyrolysis of a hyperbranched polysilyne, poly[1,1′-ferrocenylene(methyl)silyne] (**1**), at high temperature in inert atmosphere produces nonostructured ceramics (**2**) in ∼ 48–62% yields. The ceramic products **2** are characterized by SEM, XPS, EDX, XRD, and SQUID. It is found that the ceramics are electrically conductive and possess a mesoporous architecture. The iron contents of **2** estimated by EDX are 36–43%. The nanocrystals formed in the ceramics produced under nitrogen **2N** are mainly α-Fe_2O_3 whereas those in the ceramics produced under argon **2A** are mainly Fe_3Si. When magnetized by an external field at room temperature, **2A** exhibits a high saturation magnetization ($M_s \sim 49$ emu/g) and near-zero remanence and coercivity. © 2001 Elsevier Science B.V. All rights reserved.

Keywords: Hyperbranched polymers; Polysilynes; Polymer precursors; Ceramics; Nanoclusters; Ferromagnetic materials

1. Introduction

The research activity in the synthesis of organometallic polymer precursors and their controlled pyrolysis to ceramic materials has opened up a new branch of macromolecules—preceramic polymer chemistry. The polymer precursor route offers advantages such as diversity in chemical compositions, processability for bulk ceramic bodies of complex shapes, and feasibility of generating nanodimensional structures. Most studies in the preceramic polymer chemistry have been so far concentrated on structural ceramics with outstanding mechanical properties. Incorporation of nanoclusters of transition metals into ceramics may lead to the development of novel nanostructured materials with unique magnetic, electrical, and optical properties. Such possibility has been, however, virtually unexplored.

We have recently synthesized a series of new hyperbranched iron- and silicon-containing organometallic polymers, poly[1,1′-ferrocenylene(*n*-alkyl)silynes], by the polymerizations of 1,1′-dilithioferrocene ($FcLi_2$) with *n*-alkyltrichlorosilanes [$(C_nH_{2n+1})Cl_3Si$; $n = 1, 8, 12, 16, 18$] [1,2]. The reaction scheme for one of the polysilynes,
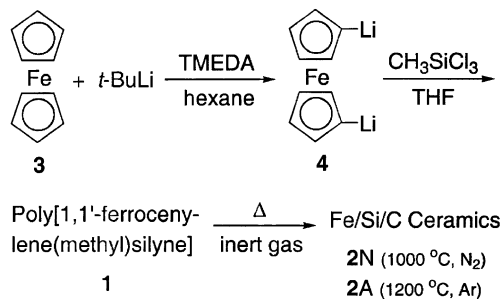
poly[1,1′-ferrocenylene(methyl)silyne] (**1**), is given in Scheme 1. In the hyperbranched polymer **1**, every one of the silicon atoms is surrounded on the average by 3/2 (or 1.5) ferrocenylene moieties, and **1** thus possesses a high theoretical iron content. The three-dimensional molecular structure of **1** may suppress the iron loss caused by volatilization, enhance the chances for the iron atoms to participate in the network formation, and hence increase the iron content of the ceramic end products.

With these considerations in mind, in this work, we investigated ceramization of the hyperbranched polysilynes. The pyrolysis of **1** produces ceramics **2**, which possess mesoporous morphologies, contain large amounts of iron nanoclusters, and exhibit soft ferromagnetism with negligibly small hysteresis loss.

2. Experimental

The synthetic details of hyperbranched poly[1,1′-ferrocenylene(n-alkyl)silynes] were reported elsewhere [1,2]. Thermogravimetric analyses (TGA) were performed on a Perkin-Elmer TGA 7 at a heating rate of 10 °C/min under nitrogen. Morphologies of the ceramics were observed on a JEOL 6300 scanning electron microscope (SEM) operating at an accelerating voltage of 5 kV, and the as-prepared ceramics were directly used in the SEM analysis without

Scheme 1.

Fig. 1. SEM photomicrograph of ceramic **2**A prepared by pyrolysis of **1** at 1200 °C under argon; scale bar: 1 μm (1000 nm).

coating with gold metal. Energy-dispersion X-ray (EDX) analyses were performed on a Philips XL30 SEM system with quantitative elemental mapping and line scan capacities operating at an accelerating voltage of 15 kV. X-ray photoelectron spectroscopy (XPS) measurements were conducted on a PHI 5600 spectrometer (Physical Electronics) and the core level spectra were measured using a monochromatic Al K_α X-ray source ($h\upsilon = 1486.6$ eV). The analyzer was operated at 23.5 eV pass energy. Binding energies were referenced to the adventitious hydrocarbon C $1s$ line at 285.0 eV and curve fitting of the XPS spectra was performed using the least square method [3]. X-ray diffraction (XRD) diagrams were recorded on a Philips PW 1830 powder diffractometer using monochromatized X-ray beam from a nickel-filtered Cu K_α radiation ($\lambda = 1.5406$ Å). Magnetization measurements were carried out using a superconducting quantum interference device (SQUID) magnetometer (Quantum Design MPMS-5S) at fields ranging from 0 to 20 kOe and at temperatures of 5 and 300 K.

In a typical pyrolysis experiment conducted under nitrogen, 28 mg of **1** was placed in a sample cell of Perkin-Elmer TGA 7 analyzer. The sample was heated to 1000 °C at a heating rate of 10 °C/min and calcinated at the highest temperature for 1 h. A ball-shaped ceramic product was obtained in ∼50% yield (referred to as **2**N with "N" standing for "nitrogen"). In another typical pyrolysis experiment carried out under argon, ∼40 mg of **1** was placed in a quartz tube in a Winston-Salem Thermcraft furnace, which was heated to 1200 °C at a heating rate of 10 °C/min in a stream of argon. The sample was sintered at the temperature for 1 h, which gave a ceramic product in ∼50% yield (**2**A; "A" standing for "argon").

3. Results and discussion

We first used TGA to investigate the pyrolysis of the hyperbranched polysilynes under nitrogen. When $n = 1$ (**1**), the pyrolysis gives a golden-colored ball-shaped ceramic product in the TGA cell in ∼50% yield. The ceramic yields of **1** vary in the range of ∼48–62% from batch to batch but are all higher than that (∼36%) of its linear counterpart poly[1,1′-ferrocenylene(dimethyl)sily-

lene] (**5**) [4,5]. The pyrolysis yield monotonically decreases with an increase in the length of the alkyl chain. When n is increased to 12, the ceramic yields decrease to ∼35–43%, which are, however, still more than two times higher than that (∼17%) of its linear cousin with a similar number of carbon atoms, e.g. poly[1,1′-ferrocenylene(diphenyl)silylene] [4]. Clearly, the hyperbranched polymers are superior to the linear ones in terms of thermolytic conversion to ceramic products. Cutting the backbone of a linear polymer a few times will quickly decrease its molecular weight, and volatilization of the low molecular weight fragments leads to a low ceramic yield [6]. On the other hand, breaking a few bonds of a hyperbranched polymer may not easily change its polymeric nature because of its three-dimensional molecular architecture. Therefore, higher ceramic yields are obtained.

Since the polymer with the shortest alkyl chain length ($n = 1$; **1**) gives the highest ceramic yields among all the hyperbranched poly[1,1-ferrocenylene(n-alkyl)silynes], we concentrated our research efforts on the ceramic materials from **1** and further studied its ceramization behaviors. When the samples of **1** are pyrolyzed in a furnace at 1200 °C in a stream of argon, high ceramic yields (∼50–60%) are again obtained, confirming that the efficient ceramization is an intrinsic property of the hyperbranched polymer.

The SEM measurements of the ceramic products can be carried out without coating with gold metal. The clear

Table 1
Atomic composition of ceramics **2** estimated by XPS and EDX analyses

Ceramic	Atomic composition (%)			
	Fe	Si	C	O
2N (XPS)	6.1	0.7	78.0	15.2
(EDX)	36.0	24.4	30.2	9.4
2A (XPS)	3.8	0.6	86.7	8.9
(EDX)	43.2	29.1	22.4	5.3
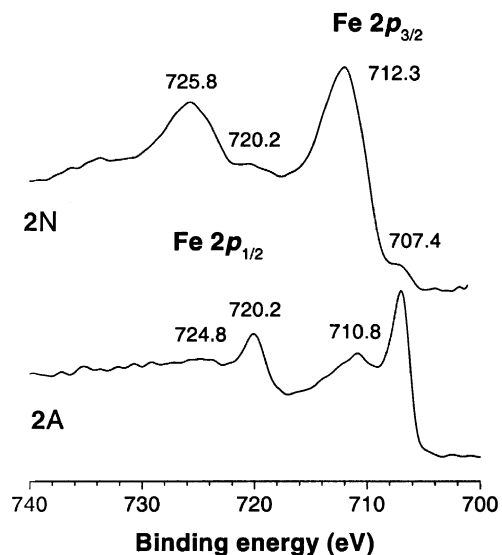
Fig. 2. Fe 2p photoelectron spectra of ceramics **2N** and **2A**.

Fig. 3. Si 2p photoelectron spectra of ceramics (A) **2N** and (B) **2A**; inset (C): curve fitting of spectrum B.
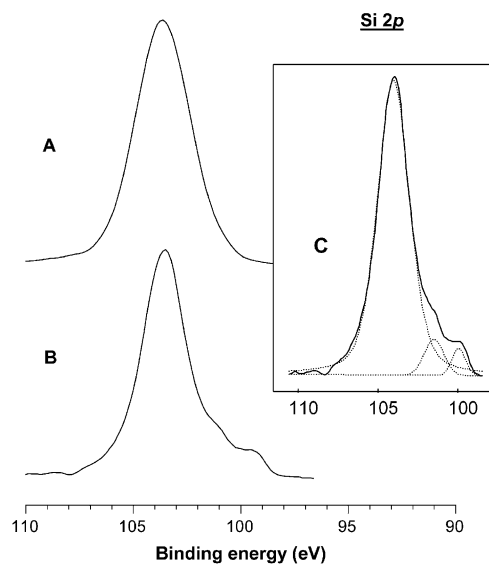
images of the SEM photomicrographs indicate that the ceramics are electrically highly conductive, suggesting the existence of conductive graphite carbon and metallic iron species in the ceramic products. As can be seen from Fig. 1, the ceramic looks like a coral reef, in which the continuous skeletons are running through a mass of "islands" or clusters, many of which have sizes of a few hundred nanometers. On the two-dimensional imaging plane, the nanoclusters are separated by mesoscopic pores, but three-dimensionally they are all tortuously interconnected, with the continuous skeletons providing the architectural support. Evidently, the coral reef-like mesoporous structure is generated by the fast simultaneous evaporation of volatile organics and agglomeration of the inorganic elements in the pyrolysis process.

We used XPS spectroscopy to estimate the surface composition of the ceramic products. The XPS analysis finds four elements on the ceramic surface, namely, iron, silicon, carbon, and oxygen (Table 1). The Fe, Si, and C elements are understandably from the polymer precursor. The oxygenic species may be introduced by the moisture absorbed by the polymer samples prior to pyrolysis and/or by the post-oxidation of the mesoporous ceramics during the handling and storage processes. The amounts of the Fe

and Si elements in the bulk of the ceramics detected by the EDX analysis are much higher than those on the surface. On the other hand, there are smaller quantities of elemental C and O in the bulk than on the surface. This suggests that the ceramization process starts from the pyrolysis-induced formation of the inorganic metallic species. The nanoclusters shown in Fig. 1 thus may be imagined as iron–silicon inner cores coated with carbonic and oxide outer layers.

An important piece of information offered by the elemental analyses is that both the ceramics prepared under nitrogen (**2N**) and argon (**2A**) comprise large amounts of elemental iron (3.8–6.1% by XPS and 36–43% by EDX), much higher than those (1.0% by XPS and 11% by EDX) in the ceramic prepared by the pyrolysis of the linear polymer **5** at a similarly high temperature (1000 °C) [4]. The ferrocenylene moieties of **1** are confined in the roughly spherical cage of the hyperbranched polysilyne, allowing the iron species to have more time to take part in the cross-linking reaction, hence enhancing their chances to transform into nonvolatile inorganic structures.

The valence shell electrons are known to contribute to the net force experienced by the core level electrons, and the core-level binding energies thus change with the change in the chemical environments [7]. We inspected the Fe 2p core level photoelectron spectra of **2** (Fig. 2) in an effort to

Table 2
Binding energies of Fe 2p core levels in ceramics **2** and other Fe-containing materials

Material	Binding energy (eV)						Reference
	Fe 2$p_{3/2}$			Fe 2$p_{1/2}$			
2	707.4	710.8	712.3	720.2	724.8	725.8	This work
Fe	707.3			720.3			[8]
Fe$_3$Si	707.5						[8–10]
Fe$_3$O$_4$		710.8			724.7		[7]
Fe$_2$O$_3$			711.6			725.1	[7]

Table 3
Binding energies of Si 2p core levels in ceramics **2** and other Si-containing materials

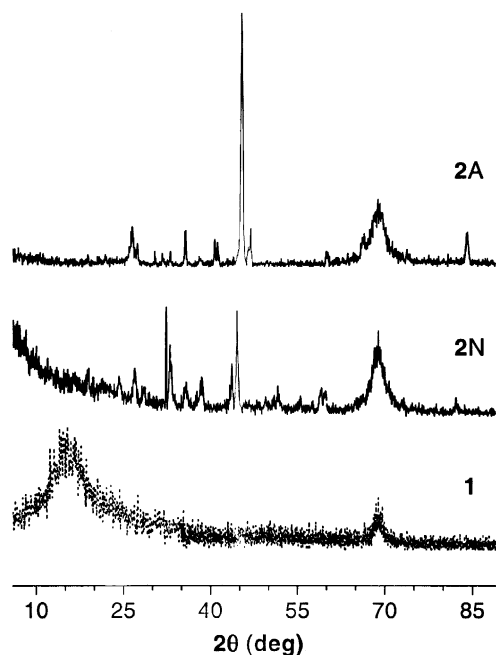| Material	Binding energy (eV)			Reference
2	104.0	101.5	99.9	This work
SiO$_2$	104.2			[11]
SiC		101.1		[12]
Fe$_3$Si			99.7	[13]

Fig. 4. XRD patterns of poly[1,1′-ferrocenylene(methyl)silyne] **1** and its ceramic products **2N** and **2A**.

understand the chemical structure of the iron species in the ceramic products. The spectrum of **2**N shows a small peak at 707.4 eV, which may be assigned to the Fe $2p_{3/2}$ core-level binding energy of Fe and Fe_3Si, because the literature data for the two iron species are almost identical, being respectively 707.3 and 707.5 eV (Table 2) [8,9]. Allen et al. [8] and Fradley [9] reported a binding energy of

720.3 eV for the Fe $2p_{1/2}$ line, and the peak at 720.2 eV in Fig. 2 thus further confirms the existence of the elemental iron in its metallic form in **6**N. Mills and Sullivan [7] reported binding energies of 711.6 and 725.1 eV for the Fe $2p_{3/2}$ and Fe $2p_{1/2}$ peaks, respectively. The intense peaks at 712.3 and 725.8 eV in Fig. 2 are thus likely to result from the Fe_2O_3 nanoclusters in **2**N. It is known that α- and γ-Fe_2O_3 species possess the same binding energy [3,10], and it is thus difficult to distinguish whether the iron oxide in **2**N is in the α- or γ-form on the basis of the XPS data alone.

The Fe $2p$ spectrum of **2**A is, however, remarkably different from that of **2**N. The Fe and Fe_3Si species give sharp intense peaks at 707.4 (Fe $2p_{3/2}$) and 720.2 eV (Fe $2p_{1/2}$). The oxide can be assigned as Fe_3O_4, because the observed binding energies for the Fe $2p_{3/2}$ (710.8 eV) and Fe $2p_{1/2}$ peaks (724.8 eV) are almost identical to those (710.8 and 724.7 eV, respectively) of Fe_3O_4 reported by Mills and Sullivan [7]. The Fe $2p_{3/2}$ envelope tails into the high binding energy region, suggesting that a small amount of Fe_2O_3 also exists in **2**A.

The Si $2p$ core level spectrum of **2**N gives an intense peak at 104.0 eV (Fig. 3A), thus the silicon in **2**N is oxidized and exists in the form of SiO_2 (Table 3). There is no obvious signal associated with iron silicide (Fe_3Si), possibly because the weak signal is buried under the overwhelming SiO_2 peak. The signal related to the Fe_3Si species is, however, detected in **2**A. The Si $2p$ spectrum of **2**A exhibits structured tails in the low binding energy region, in addition to the main peak for SiO_2 (Si^{4+}) at 104.0 eV. Using the least-square peak fitting program, it is

Table 4
Nanocrystals in ceramics **2** identified by XRD analysis

No.	Crystal	2θ (°)/d spacing (Å)[a]		ICDD file
		2N[b]	2A[c]	
1	Fe	43.65/2.07 (2.08)		31-0619
2	Fe_3Si	44.55/2.03 (2.00)	45.40/2.00 (2.00), 66.35/1.41 (1.41), 84.15/1.15 (1.15)	45-1207
3	Fe_3O_4		35.48/2.53 (2.53)	75-1372
4	α-Fe_2O_3	33.00/2.71 (2.70), 35.65/2.52 (2.52), 49.50/1.84 (1.84), 54.75/1.68 (1.69)	33.00/2.71 (2.70)	33-0664
5	γ-Fe_2O_3	35.65/2.52 (2.51), 57.50/1.60 (1.60)		25-1402
6	SiO_2	28.45/3.13 (3.11)[d]	30.40/2.94 (2.94)[e]	d,e
7	SiC	35.65/2.52 (2.51), 59.85/1.54 (1.54)[f]	35.48/2.53 (2.53), 38.05/2.36 (2.37), 59.95/1.54 (1.55)[g]	f,g
8	C	26.90/3.31 (3.35)[h]	26.50/3.36 (3.35)[h]	h

[a]The values given in the parentheses are taken from the powder diffraction files of the database of the International Center for Diffraction Data (ICDD).

[b]Sintered under nitrogen at 1000 °C for 1 h.

[c]Sintered under argon at 1200 °C for 1 h.

[d]Coesite; ICDD data file 72-1601.

[e]Stishovite; ICDD data file 72-2310.

[f]Carborundum; ICDD data file 73-1708.

[g]ICDD data file 75-1541.

[h]Graphite; ICDD data file 75-2078.

resolved that the tails are the Si $2p$ peaks for the reduced silicon species of SiC (101.5 eV) and Fe_3Si (99.9 eV) [11–13] (Fig. 3C and Table 3).

We used XRD diffratometry to examine the bulk composition and crystal structure of the ceramic products. The precursor polymer **1** is amorphous, exhibiting no sharp reflection peaks but a diffuse halo in the 2θ angle region of ~ 5–30° (Fig. 4; noticing that the broad peak centered at 2θ angle of ~ 69° is not from **1** but from the silicon wafer used in the XRD measurement). In contrast, its ceramic products **2** show diffraction patterns with numerous Bragg reflections; that is, **2** contains many crystalline species. The crystals are, however, small in size, as evidenced by the line broadening of the XRD diagrams. Using the Scherrer equation [14], it is estimated that the sizes of the crystals are in the range of 41–117 nm. The sizes of the nanocrystals are smaller than those estimated from the SEM image, suggesting that the nanocrystals coexist with other species in the nanoclusters. In other words, the nanoclusters are not pure in composition but are mixtures of different species, in agreement with the XPS and EDX results discussed above.

We used the data files in the database of the Joint Committee on Powder Diffraction Standards of the International Center for Diffraction Data (JCPDS-ICDD) to identify the nanocrystals, and the results are summarized in Table 4. The ceramic **2N** shows reflection peaks of Fe and Fe_3Si crystals at $2\theta = 43.65°$ and 44.55°, respectively. Their secondary reflections can, however, not be detected, probably due to the imperfect packing structure of the nanocrystals [14]. The diffraction diagram of **2N** displays a peak of α-Fe_2O_3 at $2\theta = 33.00°$, whose higher-order reflections are observed at 35.65°, 49.50°, and 54.75°, implying that the α-Fe_2O_3 nanocrystal in **2N** still holds a regular packing structure (Table 4, no. 4). The reflection peaks associated with the γ form of Fe_2O_3 at 35.65° and 57.50° are, however, weak in intensity. Thus, while the XPS analysis provided no clear information on the crystal polymorph, the XRD analysis here reveals that the Fe_2O_3 nanocrystals exist mainly in the α form. The reflection peaks of SiO_2, SiC, and C are all weak and broad, probably because the majority of the silicon and carbon species is in the irregular amorphous state.

In the XRD diagram of **2A**, we cannot find any peaks associated with the reflections of Fe metal. An intense peak of the Fe_3Si nanocrystal is, however, observed at 45.40°, whose higher-order reflections are clearly identifiable at 66.35° and 84.15°. Thus, most, if not all, of the iron species in **2A** exist in the form of Fe_3Si. Consistent with the XPS data, **2A** shows a Fe_3O_4 peak of moderate intensity at 35.48° but only a weak peak of α-Fe_2O_3 at 33.00°. This is in contrast to the XRD diffraction pattern of **2N**, in which no Fe_3O_4 but α-Fe_2O_3 peaks are observed (Table 4, nos. 3–4). The reflections of the SiO_2, SiC, and C species in **2A** are again weak and broad, probably due to the same reasons as discussed above for **2N**.

The ceramic products **2** can be readily attracted to a bar magnet at room temperature; that is, they are readily magnetizable. We thus used the SQUID technique to investigate their magnetization behaviors in magnetic fields. As shown in the upper panel of Fig. 5, at 300 K, **2N** is magnetized even when a weak magnetic field is applied. Its magnetization increases with an increase in the strength of the applied field and becomes saturated at ~ 16 emu/g when the external field reaches ~ 2 kOe. Its M_s increases to ~ 21 emu/g when the temperature is decreased to 5 K. The M_s for **2A** at this temperature is, however, ~ 51 emu/g, which is ~ 2.5-fold higher than that for **2N**. The XPS and XRD analyses have revealed that Fe_3Si is the major component of the nanocrystals in **2A**, while in **2N**, the nanocrystals are mainly α-Fe_2O_3, with γ-Fe_2O_3, Fe, and Fe_3Si existing in relatively small quantities. Fe_3Si, γ-Fe_2O_3, and Fe are the best-known magnetic materials but α-Fe_2O_3 is only weakly magnetic [15]; **2A** thus should show higher magnetizability than **2N**. The SQUID measurements prove that this is indeed the case, reinforcing the composition analyses of the ceramics by the XPS, EDX, and XRD techniques.

When the portion of the magnetization plots in the low field region is enlarged, the hysteresis loops of **2N** become
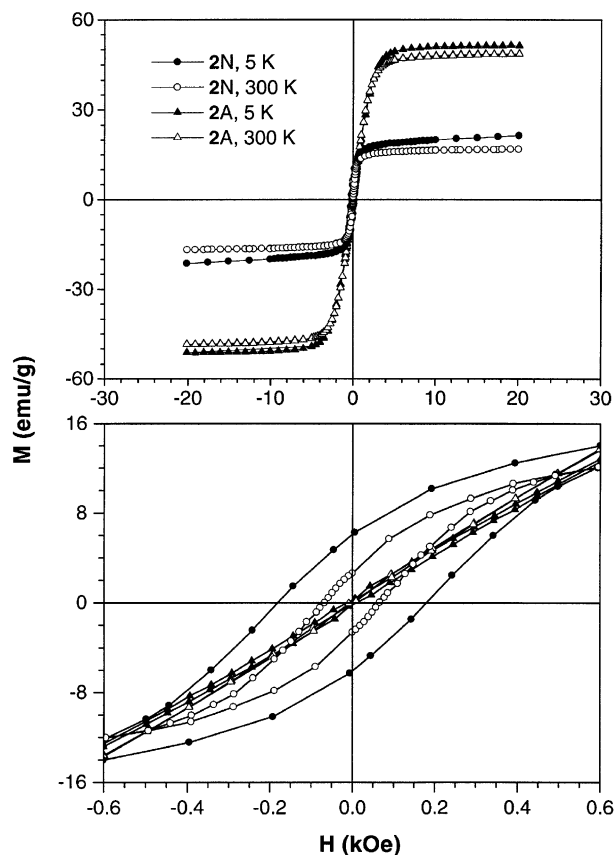

Fig. 5. Plots of magnetization (M) versus applied magnetic field (H) at 5 and 300 K for ceramics **2N** and **2A**, the lower panel being the enlarged part of the magnetization curves in the low magnetic field region.

clearly visible. The remanence and coercivity of **2**N are possibly due to the contribution from its γ-Fe_2O_3 component. Interestingly, however, even at the high magnification, **2**A does not seem to exhibit any hysteresis loops and its magnetization curves nearly cross the zero point (i.e. $M_r \sim 0$, $H_c \sim 0$), when the magnetization experiments are carried out at both 300 and 5 K. Silicon steel (Si–Fe) is widely used in electromagnetic systems because of its extremely low magnetic hysteresis loss. The near-zero M_r and H_c values of **2**A are easy to understand because Fe_3Si is the major component of the nanocrystals in the ceramic product. Thus, **2**A is an excellent soft ferromagnetic material with a high magnetic susceptibility and low hysteresis loss.

4. Conclusions

We have successfully prepared nanostructured magneto-ceramic materials using hyperbranched organometallic polymer precursors. Our finding in this study can be summarized as follows: (1) the ceramization yield increases with a decrease in the alkyl chain length of the hyperbranched poly[1,1′-ferrocenylene(*n*-alkyl)silyne] precursors, with the highest yield obtained in the polymer with the smallest alkyl (methyl) group; (2) the hyperbranched polysilynes are superior to their linear polysilylene counterparts in terms of the pyrolytic conversion to inorganic networks and the retention of elemental iron in the ceramic products; (3) the simultaneous evaporation of volatile organics and agglomeration of inorganic elements in the pyrolysis of **1** readily generates a three-dimensional mesoporous network of nanoclusters; and (4) the iron silicide nanocrystals make **2**A an excellent soft ferromagnetic material, exhibiting a high magnetizability and a negligibly small hysteresis loss.

References

[1] Q. Sun, B.Z. Tang, Polym. Prepr. 40-2 (1999) 657.
[2] Q. Sun, B.Z. Tang, Polym. Mater. Sci. Eng. 82 (2000) 105.
[3] N.S. McIntyre, D.G. Zetaruk, Anal. Chem. 49 (1977) 1521.
[4] R. Petersen, D.A. Foucher, B.Z. Tang, A. Lough, N. Raju, J. Greedan, I. Manners, Chem. Mater. 7 (1995) 2045.
[5] B.Z. Tang, R. Petersen, D.A. Foucher, A. Lough, N. Coombs, R. Sodhi, I. Manners, J. Chem. Soc., Chem. Commun. (1993) 523.
[6] W.H. Atwell, in: J.M. Ziegler, F.W.G. Fearon (Eds.), American Chemical Society, Washington, DC, Silicon-Based Polymer Science, Chap. 32 1990.
[7] P. Mills, J.L. Sullivan, J. Phys. D: Appl. Phys. 16 (1983) 723.
[8] G. Allen, M. Curtis, A.J. Hopper, P.M. Tucker, J. Chem. Soc. Dalton Trans. 14 (1974) 1525.
[9] C.S. Fradley, in: D.A. Shirley (Ed.), Electron Spectroscopy, North Holland, Amsterdam, 1972, pp. 781–801.
[10] J. Chastain, Handbook of X-ray Photoelectron Spectroscopy, Perkin-Elmer, Eden Prairie, MN, 1992.
[11] J.N. Zhou, A. Butera, H. Jiang, D.H. Yang, J.A. Barnard, J. Appl. Phys. 85 (1999) 6151.
[12] C. Senemaud, A. Gheorghiu-de La Rocque, G. Dufour, N. Herlin, J. Appl. Phys. 84 (1998) 4945.
[13] I.N. Shabanova, V.A. Trapeznikov, J. Electr. Spectrosc. Relat. Phenom. 6 (1975) 297.
[14] A. Guinier, X-Ray Diffraction in Crystals, Imperfect Crystals, and Amorphous Bodies, Dover, New York, 1994.
[15] C. Pham-Huu, C. Estournes, B. Heinrich, M.J. Ledoux, J. Chem. Soc., Faraday Trans. 94 (1998) 435.